Finite element analysis of stress evolution during the high temperature oxidation of Ni30Cr+ Cr2O3 systems

Zhimao Wang, Jean-Luc Grosseau-Poussard, Benoît Panicaud, Carl Labergère

Finite element analysis of stress evolution during the high temperature oxidation of Ni30Cr + Cr_2O_3 systems

Zhimao Wang [1], Jean-Luc Grosseau-Poussard [2], Benoît Panicaud [1*], Carl Labergère [1]

[1] Université de Technologie de Troyes (UTT), Institut Charles Delaunay (ICD), Systèmes Mécaniques et d'Ingénierie Simultanée (LASMIS), 12 rue Marie Curie, CS 42060, 10004, Troyes Cedex, France;

[2] Laboratoire des Sciences de l'Ingénieur pour l'Environnement (LaSIE), Université de La Rochelle, CNRS UMR 7356, Avenue Michel Crépeau, 17042, La Rochelle Cedex 1, France;

* Corresponding author: benoit.panicaud@utt.fr; Tel.: +333 25 71 80 61

Received: date; Accepted: date; Published: date

Abstract: The present article describes the finite element analysis of mechanical evolution during high temperature oxidation of a metallic alloy. The concerned phenomena are the stress evolutions with time and space in Ni30Cr + Cr_2O_3 system during oxidation in the range 800 to 1000°C. The forming of an oxide layer on chromium-based alloys in oxidizing environments for high temperature applications provides a good protection against further oxidation. During this oxidation, stresses develop in both oxide layer and metallic substrate, which may cause further layer cracking or spallation and limit the lifetime of alloys in such a challenging environment. In order to investigate the stress distributions, a full thermomechanical model is implemented in the commercial finite element software Abaqus/Standard through a UMAT FORTRAN subroutine. The time-dependent stress is especially calculated and compared to experimental results from bibliography. Different temperatures are considered to estimate their influence on the different phenomena and quantities of the mechanical state. Numerical values of stresses as well as for material parameters are provided in this study.

Keywords: High temperature oxidation; Thermomechanical modelling; NiCr alloy; Chromium profile; Finite Element Analysis.

1. Introduction

An oxide layer usually develops during the oxidation of a metallic alloy in high temperature oxidizing environments. Chromium-based alloys generally form an oxide layer (Cr_2O_3) in challenging environments such as nuclear power plants, thermal power plants, gas turbines, etc. Residual stresses occur because of incompatibilities between the oxide layer and the metallic substrate when such an oxide layer grows from the surface [1-3]. These residual stresses can further affect the structure and the lifetime of the metal [1-3]. Over the last few years, many studies were concentrated on the

thermomechanical modelling of NiCr alloy [4-10]. In these studies, the in-situ stress evolution in the oxide layer was investigated for different thermal loadings [7]. Different parameters were numerically identified [5,6], verified and optimized [8], especially for the viscoplastic parameters and the growth strain parameter. On the same systems NiCr+Cr_2O_3, the influence of different chemical elements such as yttria or zirconium was also tested to see the consequences both on the oxidation kinetics and on the mechanical evolution. Moreover, the stress in metal was also experimentally studied as a function of depth [9], which indicated that there is a significant stress gradient in the near metal/oxide zone in the metal side. The characteristic length of this stress gradient with depth was experimentally observed around 20 μm, which could be partially related to the outward diffusion of element Cr.

In the present article, we are interested in the simulation of stress and strain evolutions for the oxide/metal systems in relation with mechanisms of their microstructure. Previous studies have clearly identified the influence of growth parameter and viscoplastic mechanisms for the time evolution of strain and stress [5]. We presently try to use such parameters to check the finite element simulation results in comparison to experimental results. One advantage is to consider a relatively complete model adapted to our system for the whole oxidation process (heating, isothermal and cooling phases) at different temperatures. The latter parameter is systematically investigated to see its influence on the results.

Although several studies focus on the time stress evolution during the high temperature oxidation by comparing experimental measurements, there are few studies using the finite element analysis [11] and simultaneously a full thermomechanical modeling to get an accurate stress distribution in such systems. The advantages of finite element analysis are obvious [12-14], which includes:

- The finite element method can solve a thermomechanical problem under various assumptions. Therefore, it provides a low-cost tool to analyze the oxidation phenomena and predict stress evolution with time, as well as spatial distribution.
- The finite element method is flexible enough to handle and solve for very complex combinations of variables, such as inhomogeneous material properties, different kinds of boundary conditions, complex geometries, etc.
- UMAT stands for User Material, which is a subroutine defined by user himself and is called for all the material calculation points of elements. In our case, the application of UMAT provides the possibility to implement a full thermomechanical modeling in the simulation.

In some conditions, an incomplete thermomechanical modeling cannot lead to accurate enough results. The accuracy is relatively variable, based on the level of modeling and boundary conditions, whether the simulation of load conditions is realistic, etc. Thanks to previous works [4-10], a thermomechanical modeling was established and verified through experimental studies. However,

such verifications were done by considering only time evolution, without taking into account of spatial distributions of stress or strain. Moreover, in general, such a modeling only consider a single source for stress, whereas several may occur simultaneously at different spatial locations in the oxide (growth strain), as well as in the metal (chemical strain due to diffusion of species). It is thus interesting to check the influence of all these different sources, as well as the effects of spatial dimension on numerical results.

Therefore, a finite element software such as Abaqus should provide the possibility to simulate more accurately the oxidation phenomena during high temperature by applying a full thermomechanical modeling, programmed as a UMAT FORTRAN subroutine that is invoked during the calculation [15]. The details about the thermomechanical modeling is presented in section 2. In order to obtain accurate results, several works were done to identify the thermomechanical parameters [16-18], which will be introduced in section 3 as numerical input of the simulations. An introduction to UMAT subroutine interface and the division of time with the different temperature phases and adapted physical behaviors are presented in section 4. Numerical simulation results and the comparison between the simulation results and experimental results are finally investigated in section 5.

2. Thermomechanical modelling for {metal+oxide} system

In this article, a full thermomechanical modelling [6, 9] for Ni30Cr + Cr_2O_3 system is proposed to be implemented in Abaqus/Standard through a UMAT FORTRAN subroutine. This thermomechanical modeling is chosen to describe accurately the thermomechanical state, which has been wildly studied in previous works for the Ni30Cr + Cr_2O_3 systems [4-10].

2.1 Decomposition of strain

In order to clarify the equations implemented in UMAT FORTRAN subroutine, the decomposition of strain is detailled. First, we assumed that the materials properties are isotropic and homogeneous (in each materials phase), which means that it has the same properties in all directions and for all positions per material. Another hypothesis considered that for all the materials, the system has neither elastic limit nor hardening behavior, which means its behavior is directly elasto-viscoplastic, whatever the stress level is. We assume also small deformation. This is commonly considered for such systems [1-3].

2.1.1 Elastic part

The relation between the stress and the elastic strain is given by Hooke's model (Eq. 1), which can also be written as, with Lamé's coefficients λ and μ :

$$\bar{\bar{\sigma}} = \lambda \mathrm{trace}\left(\bar{\bar{\varepsilon}}^{\mathrm{elastic}}\right)\bar{\bar{I}} + 2\mu\bar{\bar{\varepsilon}}^{\mathrm{elastic}} \quad (1)$$

where $\bar{\bar{I}}$ is the second-rank identity tensor of dimension 3. The stress tensor $\bar{\bar{\sigma}}$ (Eq. 2) and elastic strain tensor $\bar{\bar{\varepsilon}}^{elastic}$ are considered as:

$$\bar{\bar{\sigma}} = \begin{pmatrix} \sigma & 0 & 0 \\ 0 & \sigma & 0 \\ 0 & 0 & \sigma_n \end{pmatrix}_B \text{ and } \bar{\bar{\varepsilon}}^{elastic} = \begin{pmatrix} \varepsilon^{elastic} & 0 & 0 \\ 0 & \varepsilon^{elastic} & 0 \\ 0 & 0 & \varepsilon^{elastic}{}_n \end{pmatrix}_B \quad (2)$$

The shear stresses are small compared to the ones for the other components in such systems that can be experimentally verified [19]. The stress tensor is concerned for the coordinates system shown in Figs. 1 and 2a. A proportional relationship between in-plane stress σ and normal stress σ_n in the metal can be also specifically assumed:

$$\sigma_n = \zeta\sigma \quad (3)$$

As proposed in [9] from experimental observations, $\zeta = 1$ as an approximation. One aim of the present study is to check such a hypothesis. It is worth noting that all components may vary with space and especially with depth (along z direction).

2.1.2 Viscoplastic part

A Norton-Hoff power law is used to simulate the viscoplastic strain $\varepsilon^{\mathrm{viscoplastic}}$, as usually considered in the metal and in the oxide for such systems [20], for an in-plane stress, with in-plane xx or yy component that is given in a rate form as:

$$\frac{d\varepsilon^{\mathrm{viscoplastic}}}{dt} = \mathrm{sign}(\sigma)J|\sigma|^N = \frac{1}{2}\mathrm{sign}(\sigma)\left(\frac{|\sigma|}{K}\right)^N \text{ and } N \in \mathbb{R} \quad (4)$$

where J and K are the creep parameters ($J = \frac{1}{2}\left(\frac{1}{K}\right)^N$) and N is the Norton exponent. $|\sigma|$ is the stress absolute value. We assume that stress release is caused mostly by creep diffusion in the oxide layer, which is regulated by the transport of chemical species along vertical grain boundaries. The same approach as described in Refs. [21-23] has been applied, with a stress exponent value N equal to unity in the Norton flow model. The Norton coefficient J for the oxide is given by:

$$J = J_{ox} = \frac{AD_0\delta\Omega}{k_B T}\left(\frac{1}{L}\right)^3 \exp\left(-\frac{Q}{RT}\right) \quad (5)$$

where A is the Coble constant without dimension, D_0 is a diffusion coefficient, δ is the grain boundary average thickness, Ω is the molar volume, k_B is Boltzmann constant, L is the grain size and Q is the activation energy of the considered mechanism.

2.1.3 Thermomechanical part

Thermal stresses are generated during the time temperature variations due to the difference of thermal expansion coefficients between the oxide layer and the metallic substrate, especially during the cooling period after oxidation. In general, the thermal expansion coefficient of the metal is higher

than that of the oxide, which means $\alpha_m > \alpha_{ox}$. Therefore, during cooling, the oxide layer is in compression and the metal is in tension. The greater is the difference between these coefficients, the more significant are the generated thermal stresses.

For thermal strain $\varepsilon^{\text{thermal}}$ in the metal and in the oxide, a classical thermal relation is considered [20]:

$$\frac{d\varepsilon^{thermal}}{dt} = \alpha(T)\frac{dT}{dt} \tag{6}$$

A rate formalism has been applied. The thermal expansion coefficient α may vary with temperature T [20] with a polynomial function:

$$\alpha(T) = b_0 - b_1 T - b_2 T^2 \tag{7}$$

where b_i are constants and thus assumed to be temperature independent. The coefficient of thermal expansion increases with temperature. b_i is different for different materials, which was verified in the thesis of Daghigh [24] for the coefficients of thermal expansion for NiCr and Cr_2O_3.

2.1.4 Growth strain part, only for oxide

In the present modelling, the Clarke's approach is used, which was originally proposed in [25], where the model is related to the microstructure configuration and especially diffusion effects with cationic or anionic fluxes, and has been verified and generalized by Panicaud et al. [10]. The growth strain rate is assumed proportional to the oxide layer kinetics:

$$\frac{\mathrm{d}\varepsilon^{\text{growth}}}{\mathrm{dt}} = \mathrm{D_{ox}(T)}\frac{\mathrm{dh_{ox}}}{\mathrm{dt}} \tag{8}$$

For the growth strain parameter $\mathrm{D_{ox}}$, it is more difficult to explicit its expression because the mechanisms depend on the considered system. For the present one, it is not yet fully established. We know that the $\mathrm{D_{ox}(T)}$ parameter depends on microstructural features and may also depend on temperature [4]. A temperature dependence $\mathrm{D_{ox}(T)}$ adapted to the used material may be:

$$\mathrm{D_{ox}^{-1}} = \mathrm{D_{ox0}^{-1}}\exp\left(-\frac{\mathrm{Q_D}}{\mathrm{RT}}\right) \tag{9}$$

where $\mathrm{D_{ox0}}$ is an initial parameter for the present oxide, as proposed in [4]. $\mathrm{Q_D}$ corresponds to an activation energy for the growth strain parameter. This $\mathrm{D_{ox}}$ parameter may be also related to the ratio of the cationic/anionic fluxes occurring within the grain boundaries when the oxide layer grows [25]. Since both fluxes follow an Arrhenius dependence, the current activation energy in Eq. 9 may be interpreted as the difference between the values associated with the anionic and cationic fluxes.

The oxide thickness $\mathrm{h_{ox}}$ follows a parabolic evolution with oxidation time t that has already been experimentally evidenced for the present material with experimental characterization by Thermal Gravimetric Analysis [4, 5]. $\mathrm{h_{ox}}$ is the thickness of the oxide layer evolving with time as:

$$\mathrm{h_{ox}} = \mathrm{Ap}\sqrt{\mathrm{t}} \tag{10}$$

$$\frac{dh_{ox}}{dt} = \frac{Ap}{2\sqrt{t}} + \frac{dAp}{dT}\frac{dT}{dt}\sqrt{t} \tag{11}$$

with Ap the parabolic kinetics parameter that may vary with temperature T.

2.1.5 Diffusion strain part, only for metal

The diffusion strain in metal layer has been studied in a previous work [9]. There has been a considerable amount of works on compositionally generated stress in materials. Such works showed that a solute atom can be treated as a source of dilatational strain. In other words, the strain depends on the concentration. Indeed, in such materials, the concentration profile indicates that the concentration of chromium strongly changes near the interface of metal and oxide layer [6-9], which has been proved to have an effect on the lattice spacing d between the crystallographic planes within the material. Therefore, we propose to associate a strain related to the chromium concentration profiles [26] as:

$$\bar{\bar{\varepsilon}}^{diffusion}(z) = \eta([Cr](z,t) - [Cr]_i)\bar{\bar{I}} \tag{12}$$

where $\bar{\bar{\varepsilon}}^{diffusion}(z)$ is the strain caused by diffusion, which is a function of z; η is a constant coefficient coupling the chromium concentration profiles to the diffusion strain; $[Cr](z,t)$ is chromium concentration profiles as a function of z; $[Cr]_i$ is the initial concentration of chromium. $\bar{\bar{I}}$ is the second-rank identity tensor of dimension 3. Stress may influence concentration profile. However, we assume this effect as a second order influence. Consequently, the chromium concentration profiles as a function of z (and time) can be solved considering the following solution:

$$[Cr](z,t) = (1-\beta)[Cr]_i erf(q) + \beta[Cr]_i \tag{13}$$

where $[Cr]_i$ is the initial concentration of chromium; and $q = \frac{z}{2\sqrt{Dt}}$. The numerical approximations of error function erf are given in [27]. β is a coefficient indicating the percentage of chromium in the metallic side to the metal/oxide interface for long time oxidation. To simplify the calculation, the ratio β is considered as a constant equal to 0.413 for the parabolic oxidation law, which is given by a calculation in the work of Whittle et al. [28]. By combining the numerical approximation and Eq. 13, an analytical solution is proposed as:

$$[Cr](z,t) = (1-\beta)[Cr]_i\left(1 - (a_1 n + a_2 n^2 + a_3 n^3 + a_4 n^4 + a_5 n^5)e^{-q^2}\right) + \beta[Cr]_i \tag{14}$$

with

$$\begin{cases} q = \dfrac{z}{2\sqrt{Dt}} \\ n = \dfrac{1}{1+pq} \\ p = 0.3275911, a_1 = 0.254829592, a_2 = -0.284496736, \\ a_3 = 1.421413741, a_4 = -1.453152027, a_5 = 1.061405429 \\ \beta = 0.413 \\ |error| \le 1.5E-7 \end{cases} \tag{15}$$

2.2 Thermomechanical modelling

To systematically ensure the continuity condition during all the oxidation time of the metal, the following assumptions have to be assumed:

- The two-dimensional effects such as rumpling are not considered.
- The non-linear mechanical phenomena (buckling, cracking, spalling) are not considered.

The displacement is continuous under specific assumptions (no delamination…). It is then possible to prove from this continuity and assuming plane interfaces that it leads to the continuity of strain. Because of the adherence between oxide layer and metallic substrate, after calculations, the continuity equation can be expressed as, for all time:

$$\varepsilon_m = \varepsilon_{ox} \tag{16}$$

The deformation decomposition is tensorial but we are only presenting the in-plane components as usually considered for such systems [1-3]. With the proposed strain decomposition, it leads to:

$$\left(\varepsilon^{\text{elastic}} + \varepsilon^{\text{viscoplastic}} + \varepsilon^{\text{thermal}} + \varepsilon^{\text{diffusion}}\right)_m = \left(\varepsilon^{\text{elastic}} + \varepsilon^{\text{viscoplastic}} + \varepsilon^{\text{thermal}} + \varepsilon^{\text{growth}}\right)_{ox} \tag{17}$$

In a rate formalism, it corresponds thus to:

$$\left(\frac{d\varepsilon^{\text{elastic}}}{dt} + \frac{d\varepsilon^{\text{viscoplastic}}}{dt} + \frac{d\varepsilon^{\text{thermal}}}{dt} + \frac{d\varepsilon^{\text{diffusion}}}{dt}\right)_m = \left(\frac{d\varepsilon^{\text{elastic}}}{dt} + \frac{d\varepsilon^{\text{viscoplastic}}}{dt} + \frac{d\varepsilon^{\text{thermal}}}{dt} + \frac{d\varepsilon^{\text{growth}}}{dt}\right)_{ox} \tag{18}$$

3. Geometry and materials parameters

3.1 Considered geometry and mesh

The investigated geometry is a three layers model, which contains an air layer, an oxide layer and a metal layer as shown in Fig. 1.

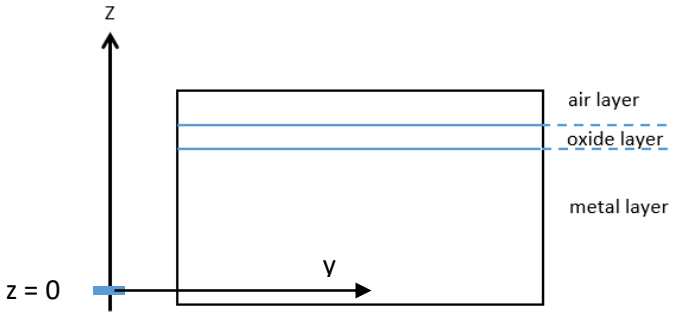

Figure 1. Illustration of the geometry for simulations

The oxide/metal geometry is supposed to have symmetrical oxidation of the two metallic sides. Because the oxidation is related to the surface, ratio of the upper and lower surfaces over side surfaces

are bigger such that we can generally neglect oxidation of these sides. Moreover, because we are mainly interested in the z variations, possible x or y variations of the quantities are often disregarded. We are presently interested to investigate these spatial variations. Besides, by applying a symmetry boundary condition at neutral plane z=0 (corresponding to the lower plane in Fig. 1), the simulation geometry is advantageously simplified. Therefore, only half of the system is considered for simulations, from top surface to neutral plane. Moreover, an air layer is added, because of the outward growth of oxide layer [16-18]. It is necessary to add it because if not, there would be no space for the growth of oxide layer, which cannot be correctly simulated. All the strains are set to be zero for the air layer, which does not affect the stress calculation for the oxide and metal layers. The simulation geometry is determinate at the beginning of the process, including the mesh type, the element number, the node number etc., which cannot be modified during simulations. As previously written, the stresses and strains in the air layer is always under control as 0 during simulations. At the initial time of simulation, the thickness of oxide layer is 1 nm in order to start from a non-zero value and avoid division by zero in Eq. (11). The layers distinction between the different chemical phases is eventually controlled by the local coordinate z (see Figs. 1 and 2a) of the integration point of each element. Spatial distribution function of z can be introduced to attribute specific behavior or properties to each chemical phase in UMAT.

Several preliminary tests were carried out before implementation of the full thermomechanical modeling. A test with rough mesh or fine mesh shows that the quality of mesh has a significant influence on the stress values, and the fine mesh gives an obvious increasing precision of results. The influence of the different strains has also been separately tested to verify that each strain part is functional in the subroutine UMAT. In order to simulate the oxidation and the near surface zone more precisely, a geometry and a fine mesh are eventually systematically applied.

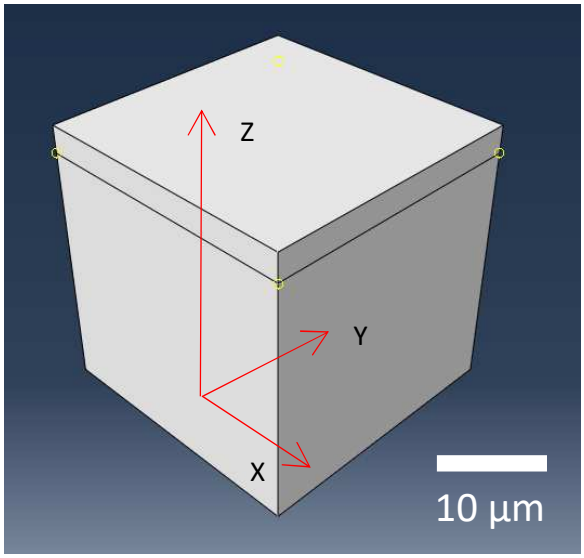

(a)

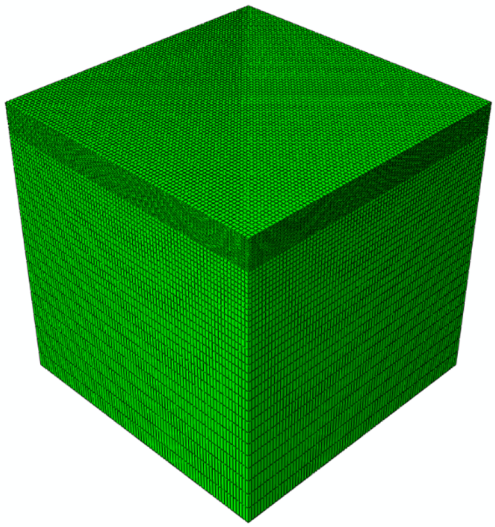

(b)

Figure 2. Geometry (a) and mesh (b). Dimensions of the simulation box are 20*20*20 μm^3

As shown in Fig. 2, in order to adapt to the oxide layer thickness, the simulation is applied to a box shape geometry, which is 20*20*20 μm^3 hexahedral element. Initially (undeformed state), along axis z, from 0 to 18 μm is the metal layer, and from 18 μm to 20 μm is the oxide + air layer (Fig. 2a). The mesh seeds set for axis x, y and z are respectively 80, 80 and 50. There are a total of 334611 nodes and 320000 elements in this geometry. For the different layers, a different mesh is considered (Fig. 2b). Refinement of the mesh is indeed required to obtain a correct accuracy. For oxide + air layer, there are 20 nodes, which means the thickness of one element is 0.1 μm that is more suitable for the simulation of oxide layer. For the metal layer, there are 30 nodes and the elements at neutral plane is 5 times thicker than the elements at the oxide/metal interface.

The element type is C3D8R for all the layers, which is an 8-node hexahedral linear reduced integration element. Compared to a full integration element, a linear reduced integration element contains only one integration point at the center of the element. The linear reduced integration element has the following advantages [29]:

(1) The shear self-locking phenomenon is relatively difficult to occur under the bending load.

(2) The results of the displacement solution are more accurate.

(3) The accuracy of the analysis is not greatly affected when the mesh is deformed.

Free boundary conditions are applied to the top surface and lateral surfaces of this geometry and the XY plane symmetry boundary condition is applied to the bottom surface. An analytical path is created along axis z at the center of this geometry, which will be systematically used to plot the depth-dependent stress. It corresponds to a straight line from coordinates in μm (10,10,0) to (10,10,20).

3.2 Input materials parameters

In the following subsections, the simulation are compared to the time-dependent stress results obtained in Tao's work [16]. In the latter, it was shown the time evolution of stresses for 800°C, 900°C, or 1000°C oxidized for 7.4 h. The parameters used correspond to Ni30Cr material, which represents 30% of the weight of Cr. The same material and parameters are presently considered. Knowing that the samples are oxidized at 800°C, 900°C or 1000°C, the input parameters for the three temperatures are shown in Table 1. As we know from other studies [16-18], for an isothermal oxidation for Ni30Cr + Cr_2O_3 systems, the stress in oxide layer increases at the beginning and relax during the oxidation process. In the work of Guerain [17], the oxidation condition is at 800°C, 900°C, or 1000°C during 20 h. However, experiments show that for the oxidation at high temperature and long time, there are cracks and spalls in the oxide layer, which are not presently considered. From a physical point of view, we

decided to simulate three oxidation conditions separately, which are oxidation at 800°C for 10h, oxidation at 900°C for 10h, or oxidation at 1000°C for 1h, whose results will be presented in section 5 and compared to the experimental results performed in [16]. The case for oxidation at 1000°C for 5h will also be considered for comparison (see section 5.4).

Table 1. The input parameters from [9, 16-18]

Oxidation condition	$\boldsymbol{Ap}$ $(\boldsymbol{mm\ s^{-1/2}})$	$\boldsymbol{E_{ox}}$ $(\boldsymbol{MPa})$	$\boldsymbol{\nu_{ox}}$	$\boldsymbol{K_{ox}}$ $(\boldsymbol{MPa\ s^{1/Nox}})$	$\boldsymbol{N_{ox}}$	$\boldsymbol{\alpha_{ox}}$ $(\boldsymbol{K^{-1}})$
800°C	2.83E-6	225000	0.29	2.65E8	1	6.99E-6
900°C	4.73E-6	215000	0.29	1.83E8	1	7.11E-6
1000°C	1.43E-5	205000	0.29	3.5E7	1	7.24E-6
	$\boldsymbol{D_{ox}}$ $(\boldsymbol{mm^{-1}})$	$\boldsymbol{E_m}$ $(\boldsymbol{MPa})$	$\boldsymbol{\nu_m}$	$\boldsymbol{K_m}$ $(\boldsymbol{MPa\ s^{1/Nm}})$	$\boldsymbol{N_m}$	$\boldsymbol{\alpha_m}$ $(\boldsymbol{K^{-1}})$
800°C	51.4	170000	0.3	2.39E11	1	1.9E-5
900°C	56.6	165000	0.3	1.05E13	1	1.96E-5
1000°C	51.9	160000	0.3	1.88E15	1	2.02E-5
	$\boldsymbol{[Cr]_0}$	H	$\boldsymbol{D}$ $(\boldsymbol{mm^2 s^{-1}})$			
800°C	0.345	-6.57E-03	2.59E-12			
900°C	0.345	-1.18E-02	4.09E-11			
1000°C	0.2828	-8.98E-03	4.19E-10			

In table 1, $\boldsymbol{Ap}$ is the kinetics coefficient of the global chemical oxidation reaction; $\boldsymbol{E_{ox}}$ corresponds to the Young's modulus of oxide layer; $\boldsymbol{\nu_{ox}}$ is the Poisson's ratio of oxide layer; $\boldsymbol{K_{ox}}$ and $\boldsymbol{N_{ox}}$ correspond to the viscoplastic parameters of oxide layer; $\boldsymbol{\alpha_{ox}}$ is the thermal expansion coefficient of oxide layer; $\boldsymbol{D_{ox}}$ corresponds to the growth strain parameter; $\boldsymbol{E_m}$ and $\boldsymbol{\nu_m}$ are the Young's modulus and the Poisson's ratio of metal layer; $\boldsymbol{K_m}$ and $\boldsymbol{N_m}$ are the viscoplastic parameters of metal layer; $\boldsymbol{\alpha_m}$ corresponds to thermal expansion coefficient of metal layer; $\boldsymbol{[Cr]_0}$ is the initial weight percentages concentration of element Cr; η corresponds to a constant coefficient coupling the chromium concentration to the diffusion strain and $\boldsymbol{D}$ is the diffusion coefficient of chromium in NiCr.

4. UMAT implementation in Abaqus/Standard

4.1 Temperature phases defined in the input file

In the input file, there is not only the geometry information but also the calculation step information, which is here called (temperature) phase. Phase means here for a time domain variation of temperature, which is a time period that corresponds to the different temperature conditions. In order to illustrate, the phases of oxidation for the case at 900°C for 10 h are presented.

To have more realistic conditions of high temperature oxidation of our samples, different temperature phases were defined and created in the input file, which are respectively temperature increase, isothermal oxidation and temperature decrease as shown in Fig. 3.

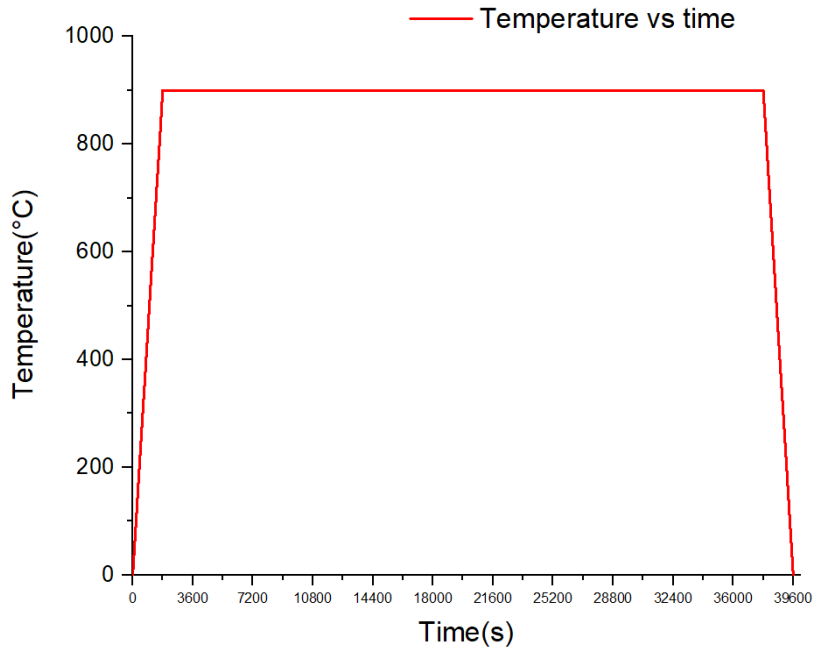

Figure 3 Oxidation temperature vs oxidation time

As shown in Fig. 3, there are three temperature phases for oxidation at 900°C for 10 h. As mentioned in section 2, the different strains in this system may include in general: $\varepsilon^{elastic}{}_m, \varepsilon^{viscoplastic}{}_m, \varepsilon^{thermal}{}_m, \quad \varepsilon^{diffusion}{}_m, \quad \varepsilon^{elastic}{}_{ox}, \varepsilon^{viscoplastic}{}_{ox}, \varepsilon^{thermal}{}_{ox}$ and $\varepsilon^{growth}{}_{ox}$. The indices "ox" and "m" refer to the oxide layer and the metal layer respectively. The calculation requires considering systematically elastic strain to relate to the stress through Hooke's model.

Phase one - temperature increases = heating process up to 900°C

The time period is from 0 to 1800 s, during which the temperature goes from 25 to 900 Celsius degrees for 30 minutes.

In this phase one, the thermal strain and elastic strain are mainly concerned and the other strains are not concerned. We assumed that during this temperature increase phase, there are neither viscoplastic strain, nor diffusion strain, nor growth strain. Compared to the isothermal phase, these strains should be negligible because duration of temperature increase phase is relatively short compared to the isothermal phase and the oxide growth is mainly developing during the next

isothermal phase, limiting the growth strain contribution. Moreover, the viscoplastic strain is more significant at high temperature. Thus, for the temperature increase phase, these strains are not considered, which is the same for the temperature decrease phase.

This phase is divided into 10 time steps. Each time step is Δt = 180 s and temperature rises ΔT = 87.5 Celsius degrees per time step. The time step and temperature step, Δt and ΔT are programmed in the input file.

Phase two - constant temperature = isothermal oxidation at 900°C

The time period is from 1800 s to 37800 s. The temperature is maintained at 900 Celsius degrees for 10h. During the simulation, the viscoplastic strain, diffusion strain, growth strain and elastic strain have to be considered. The thermal strain is no more considered because of the isothermal condition of phase two.

This phase is divided into 60 time steps. Each time step is Δt = 600 s and temperature remains at 900 Celsius degrees. In this phase, the growth of the oxide layer is concerned. As proposed in Eq. 10, it is calculated by means of the kinetics coefficient Ap and the evolving oxidation time t. The kinetics coefficient Ap is given in UMAT file and the oxidation time t is related to the temperature phase and corresponding time step.

Phase three - temperature decreases = cooling process down to 25°C

The period is from 37800 s to 39600 s, during which the temperature goes from 900 to 25 Celsius degrees in 30 minutes. In phase three, only the thermal strain and elastic strain are concerned, whereas the other strains are not concerned. As the temperature decreases, there is no more significant growth of the oxide layer because of the protective effect of the present oxide layer. The decreasing of temperature also causes the lack of activation energy for viscoplastic and diffusion phenomena. We assume thus that during the temperature decrease phase, there are neither viscoplastic strain, nor diffusion strain, nor growth strain. It is divided into 20 time steps. Each step is Δt = 90 s and temperature reduces of ΔT = -43.75 Celsius degrees per time step.

4.2 User subroutine algorithm

The detailed flowchart algorithm is illustrated in Fig.4. The first block of the proposed algorithm "Start of UMAT" is detailed in [15], which is used to define the variables. Here is the list of used variables: σ_{n+1} and σ_n are the stress matrix with 6 degrees of freedom. At the beginning of the incremental step, the values in the σ_{n+1} matrix are transferred to UMAT through the interface between UMAT and the main program. At the end of the incremental step, UMAT updates the σ_{n+1} matrix. t is the value of total time at the beginning of the current incremental step, which is used to distinguish the different temperature phases. The conditions of phases 1, 2 and 3 have been discussed in section

4.1, such as thermal strain, viscoplastic strain, growth strain and diffusion strain. COORDS(j) is an array containing the coordinates of this point with for example z = COORDS(3), and h_{ox} is the thickness of oxide layer, which are used to distinguish the air layer, oxide layer and metal layer.

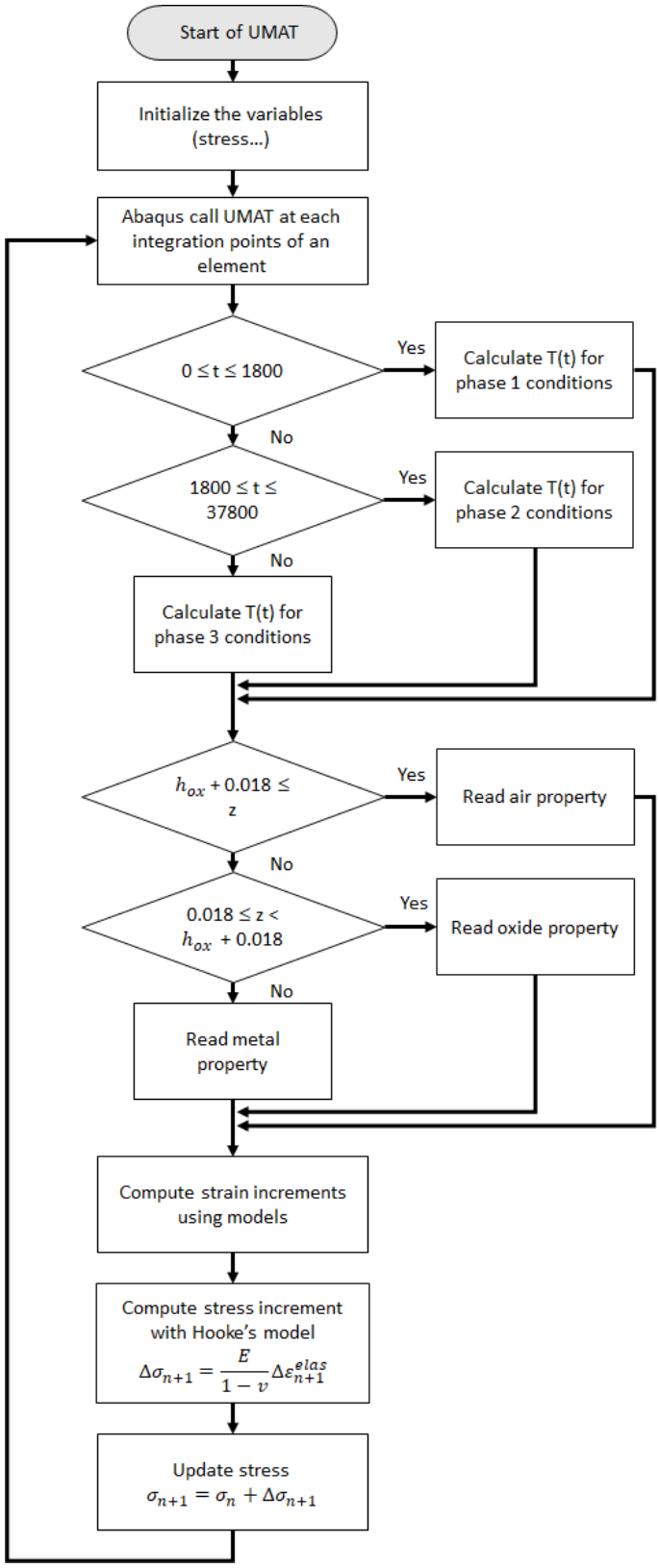

Figure 4 Flowchart of UMAT implementation (in the case of constant temperature phase of 10h ; time durations are in s and space lengths are in mm)

As shown in Fig. 4, the flowchart indicates the fundamental logic of how the UMAT works. At first, the start of UMAT means that the subroutine UMAT is compiling with the software ABAQUS/Standard through the interface Abaqus Command. In the UMAT, the stresses of the previous increment step are saved in the matrix σ_n. The stress is set to be 0 MPa for the first step of first phase.

There are two choices in the UMAT: the first one distinguishes the temperature phase conditions and the second one gives us the different material properties. Because the simulation has three temperature phases: temperature increase, constant temperature and temperature decrease, the temperature choice makes a distinction between different temperature phases according to the duration of each phase. In addition, the present system is an oxide/metal system and the outward growth phenomena of oxide layer is also simulated. Thus, we need to preset/allocate a space for the growth of oxide layer, in the present UMAT, which is called air layer. The existence of air layer does not influence the stress calculation in oxide layer and metal layer by setting the stress as 0 in air layer. According to the z coordinate of each element, the elements are divided into air layer, oxide layer and metal layer, in which are given the different properties including mechanical property, thermal property, growth property etc.

The most important part is the calculation of the strain and stress variations by using the full thermomechanical model, which has been introduced in section 2. We have considered elastic strain, viscoplastic strain, thermal strain, growth strain or diffusion strain, depending on the considered temperature phase. The elastic strain is obtained by the total strain minus the other strains, including the viscoplastic strain when considered. The total strain is obtained from the previous increment step and the viscoplastic deformation plays a role of relaxation. The calculation of the stress variation related to the elastic strain variation is specifically performed using the Hooke's model with a Jacobian matrix. At the end of this increment step, the stresses are actualized by adding the σ_n and the stress variation $\Delta\sigma_{n+1}$ together. For the present simulations, the model is established in 3D, because the samples that we experimentally studied are 3D and the results of simulations are compared to 3D experimental results. Thus, 3D simulation is more relevant to confront the reality.

5. Results and discussion

5.1 Oxidation at 800°C for 10h

By using the parameters in Table 1, the mesh and geometry of Fig. 2, the simulation results are obtained. In order to present the spatial stress distribution, the stress-field nephograms are shown in Fig. 5 and the stress distribution curves along the center path are plotted in Fig. 6.

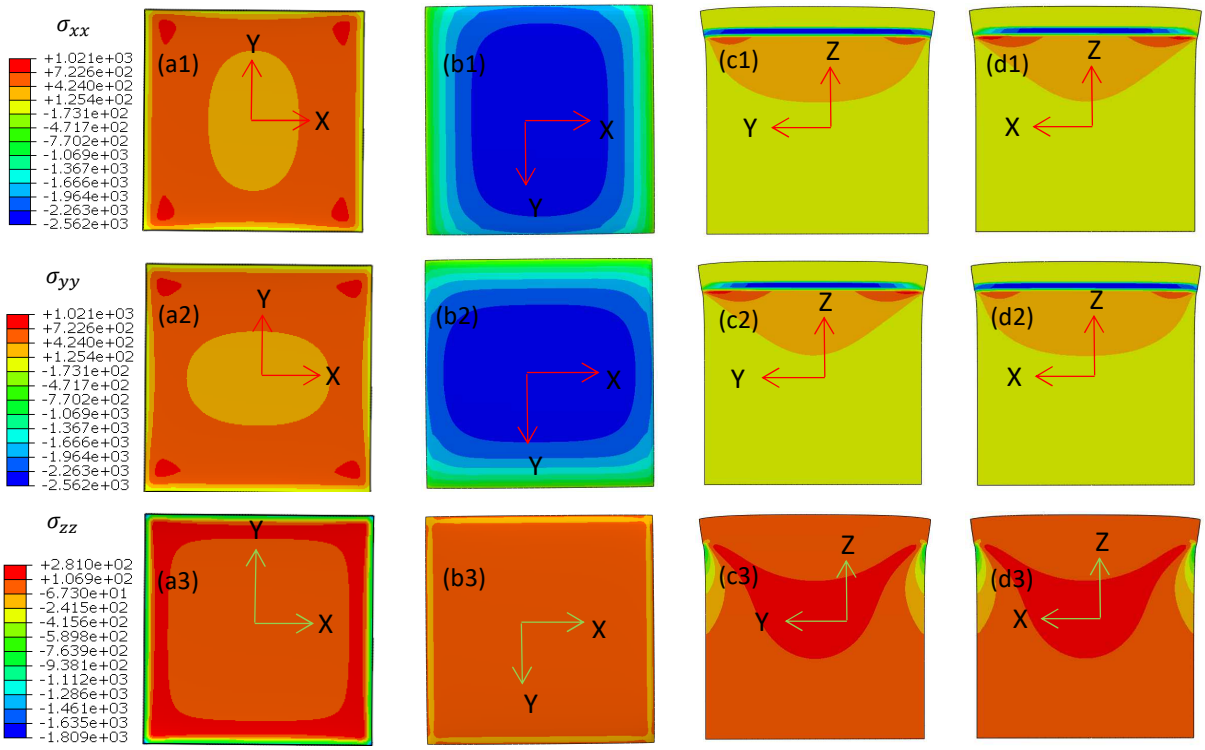

Figure 5. The stress-field nephograms (stress in MPa)

The stress-field nephograms at the end of phase 3 are presented in Fig. 5, which includes the distributions of $\boldsymbol{\sigma_{xx}}$, $\boldsymbol{\sigma_{yy}}$ and $\boldsymbol{\sigma_{zz}}$ near metal/oxide interface for metal side and oxide side, at the planes YZ and XZ. From the comparison of $\boldsymbol{\sigma_{xx}}$ and $\boldsymbol{\sigma_{yy}}$, it is shown that after rotating by 90° they are identical, which means that the in-plane stress is isotropic as expected. Isotropy of the stress should lead to $\boldsymbol{\sigma_{xx} = f(x, y = 0)}$ and $\boldsymbol{\sigma_{yy} = f(x = 0, y)}$. It thus leads to $\frac{\partial \sigma_{xx}}{\partial x} = \frac{\partial \sigma_{yy}}{\partial y}$. It corresponds to the mechanical balance. Indeed, when $\boldsymbol{\sigma_{xy} = 0}$ associated also to isotropic conditions, mechanical balance equations gives: $\frac{\partial \sigma_{xx}}{\partial x} = \mathbf{0}$ and $\frac{\partial \sigma_{yy}}{\partial y} = \mathbf{0}$ that leads to the announced equality. The corresponding stress distributions for xx and yy components satisfy thus mechanical balance according to Fig. 5.

Figs. 5(a1) to (a3) show that the stress is concentrated at the corners and edges for metal side near metal/oxide interface. Figs. 5(b1) to (b3) present the stress distribution in oxide layer. For $\boldsymbol{\sigma_{xx}}$ and $\boldsymbol{\sigma_{yy}}$, they are concentrated at the center of oxide layer and for $\boldsymbol{\sigma_{zz}}$, it only remains a low level in the oxide

layer. For the stress distribution at the different planes, the three layers system is clearly shown in Figs. 5(c1) to (c3) and Figs. 5(d1) to (d3).

The stress distributions along axis z are plotted along the center path, which are presented in Fig. 6.

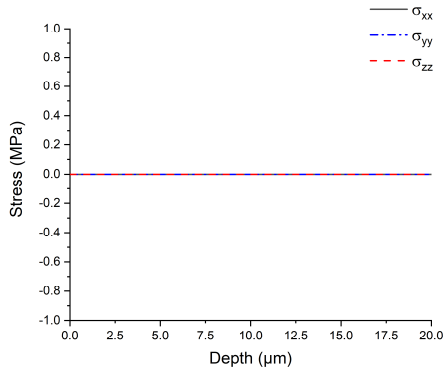

(a) end of phase 1 : temperature increase

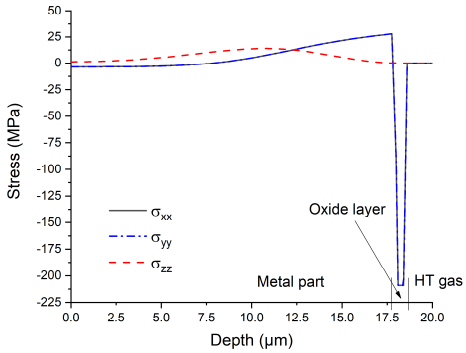

(b) end of phase 2 : constant temperature

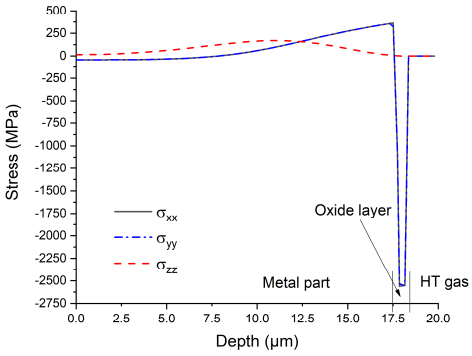

(c) end of phase 3 : temperature decrease

Figure 6. The distribution of stress components at the end of phase 1 (a), at the end of phase 2 (b), and at the end of phase 3 (c); in the deformed configuration

In these simulations, according to the model described in section 2, the distribution of stress components is calculated for the different temperature phases.

In Figs. 6 (a) to (c), the interface of metal/oxide is at depth around 17.5 μm. As shown in Figs. 6, the $\boldsymbol{\sigma_{xx}}$ and $\boldsymbol{\sigma_{yy}}$ are very close for all temperature phases, which indicates that the simulation leads to an isotropic mechanical state along this specific path. For the phase 1, the stress is zero for all components, because the growth of the oxide layer is not considered. As the thickness of the layer is very small (close to 0), it does not lead to significant stresses, even if the thermal expansion is non-zero. At the end of phase 2, the isothermal phase, the maximum absolute value for stress in the oxide layer is 209 MPa and in the metal layer is 28 MPa. At the end of phase 3, room temperature, the maximum absolute value for stress in the oxide layer is 2561 MPa and in the metal layer it is 362 MPa. For phase 2 and phase 3, the maximum stress for $\boldsymbol{\sigma_{xx}}$ and $\boldsymbol{\sigma_{yy}}$ appears near the oxide/metal interface.

The maximum absolute value for stress in the oxide layer at the room temperature corresponds to the values obtained in other works, which is around 2-2.5 GPa [16-18].

The time-dependent stress can also be plotted, which can be compared with the results obtained in the work of Tao [16], for material Ni30Cr and oxidized at 800°C for 7.4h. In Fig. 7 is presented the time-dependent stress of the first 7 hours for the experimental results and simulation results.

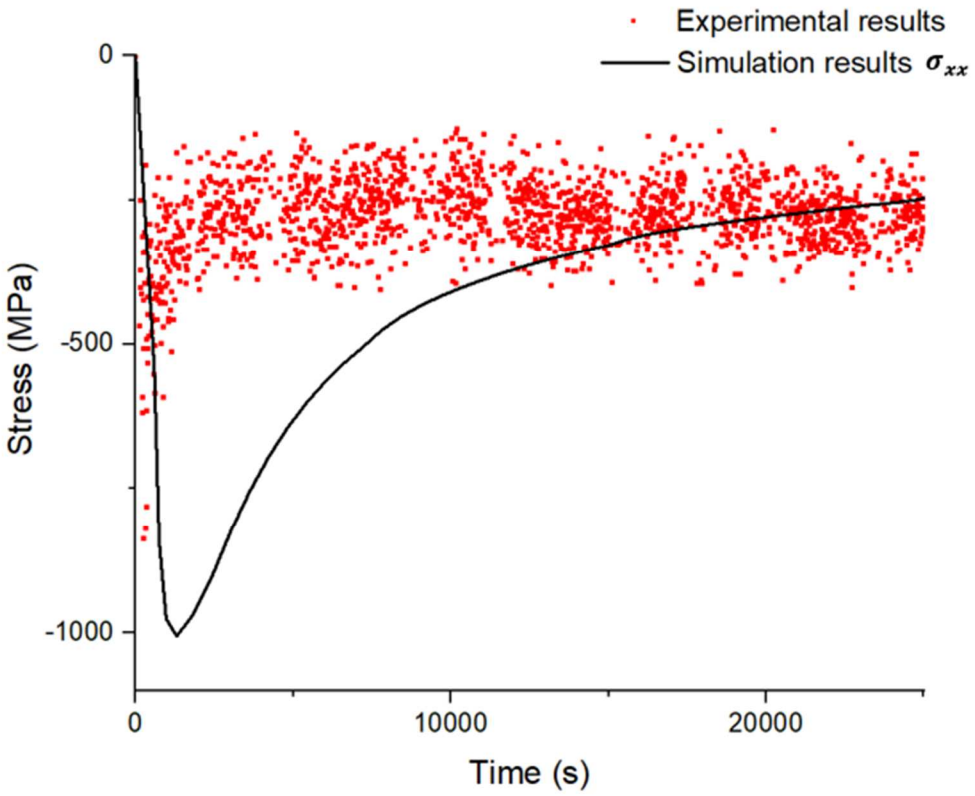

Figure 7. Time evolution of stress $\boldsymbol{\sigma_{xx}}$ for isothermal condition at 800°C

Fig. 7 shows the comparison of the time-dependence of stress for oxide layer, which includes the experimental results and the simulation results for isothermal oxidation condition at 800°C. The simulation results correspond quite well to the experimental results, especially at the end of the phase 2. For all time, the amplitude agrees well but evolution presents slight differences, especially in term of the inflection time of the minimum. For numerical simulation, it is shown that at the beginning, the absolute stress increases in the oxide layer. At the same time, the viscoplasticity causes a relaxation of stress, which finally gets a balance between the increase and relaxation parts. Therefore, the minimum stress is affected by the parameters such as the viscoplastic parameter of oxide layer $\boldsymbol{K_{ox}}$ and the growth strain parameter $\boldsymbol{D_{ox}}$.

For the delay of the inflection time, it may be caused by the different oxidation conditions for phase 1. As previously mentioned, in the numerical simulations, the viscoplastic strain, diffusion strain, and growth strain are not considered in this phase. However, in the experiments, these strains may exist, which may cause a residual stress for the isothermal phase. For the simulation, at the beginning of

phase 2, the stress is close to 0 MPa, which causes a delay of time both in the stress increase and stress relaxation.

Concerning time evolution there finally exists several differences. The main difference between the simulation results and experimental ones is thus the rate of strain relaxation. As shown in Fig.7, the stress in relaxation part evolves more quickly for experimental results than for the simulation results, which may be caused by the delay of the inflection time due to uncertainties on the knowledge of viscoplastic parameters. By modifying the viscoplastic parameters, the consistency of simulation results and experimental results could be indeed improved. Typically, when varying $\boldsymbol{K_{ox}}$ we know that an evolution is expected. A small variation of $\boldsymbol{K_{ox}}$ leads to a significant change in stress value and its evolution. However, the viscoplastic parameters cannot be easily modified without physical meaning. Moreover, the parameters used in this article have already been optimized in previous works according to some physical criteria [6, 16], taking into account the temperature influence on the relaxation parameter $\boldsymbol{K_{ox}(T)}$ by use of an inverse analysis. The present analysis concludes that the parameters may be not perfectly tuned, and it thus requires more investigations that will be done in further works.

5.2 Oxidation at 900°C for 10h

By using the parameters in Table 1, the mesh and geometry of Fig. 2, the simulation results are obtained and the stress distribution curves along the center path are plotted.

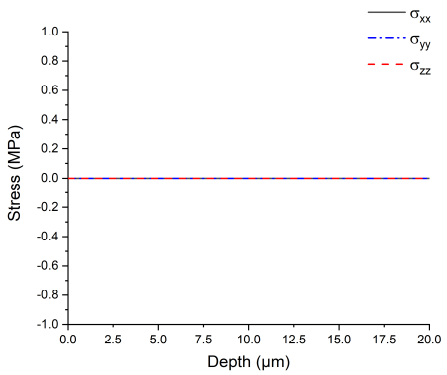

(a) end of phase 1 : temperature increase

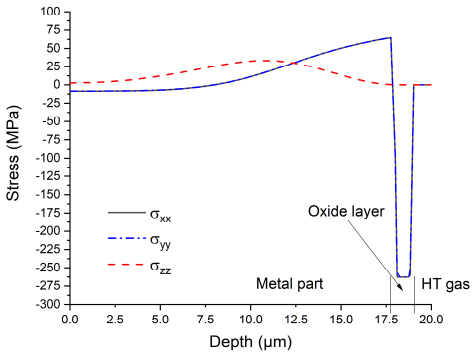

(b) end of phase 2 : constant temperature

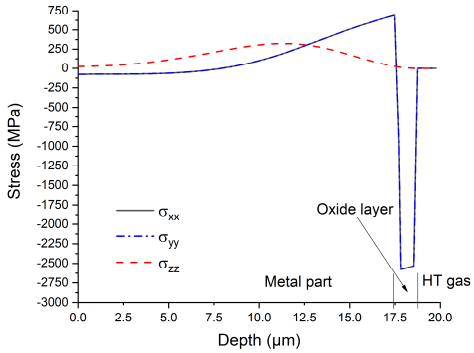

(c) end of phase 3 : temperature decrease

Figure 8. The distribution of stress components at the end of phase 1 (a), at the end of phase 2 (b), and at the end of phase 3 (c); in the deformed configuration

Fig. 8 shows the stress distribution along axis z. For Figs. 8 (a) to (c), the interface of metal/oxide is at depth around 17.5 μm. The results show that the stress in the metal layer is mainly in tension and in the oxide layer is in compression. At the end of phase 2, the maximum absolute value for stress in the oxide layer is 262 MPa and in the metal layer is 65 MPa. At the end of phase 3, room temperature, the maximum absolute value for stress in the oxide layer is 2577 MPa and in the metal layer is 691 MPa. For phase 2 and phase 3, the maximum stress for $\boldsymbol{\sigma_{xx}}$ and $\boldsymbol{\sigma_{yy}}$ appears near the oxide/metal interface.

In order to compare with the results obtained in the work of Tao [16], for material Ni30Cr and oxidized at 900°C for 7.4h, the time-dependent stress is plotted. In Fig. 9, it is shown the time-dependent stresses of the first 7 hours for the experimental and simulation results.

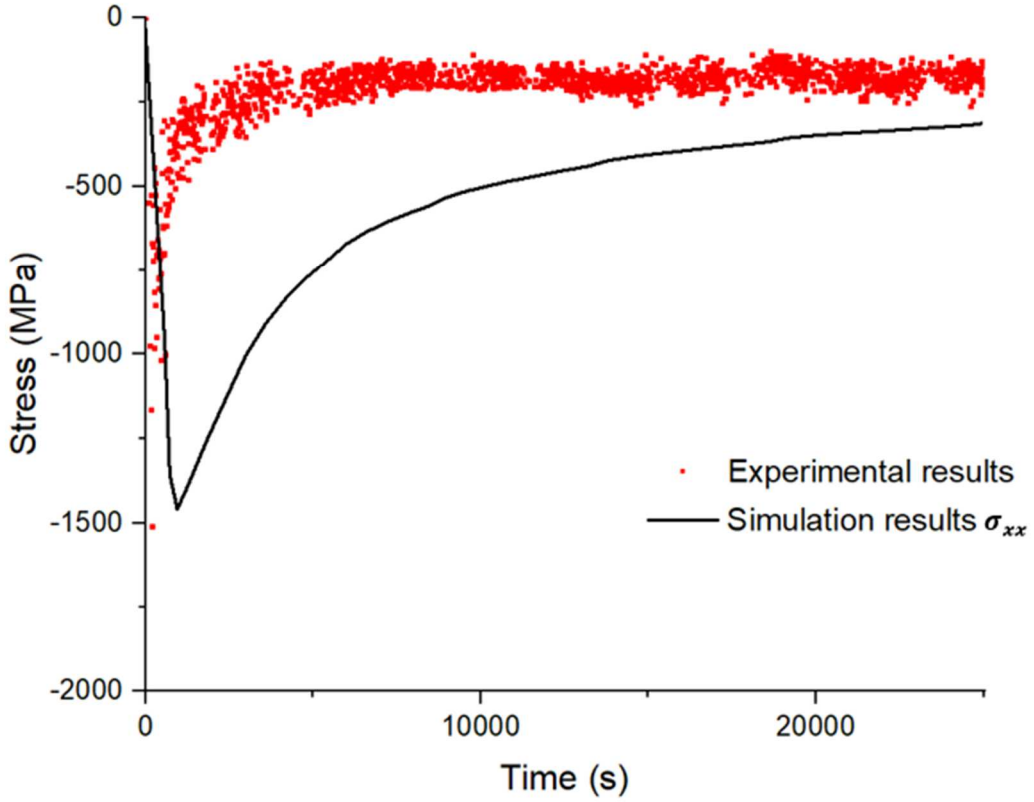

Figure 9. Time evolution of stress $\boldsymbol{\sigma_{xx}}$ for isothermal condition at 900°C

By using the given parameters in Table 1, the simulation is performed and results are shown in Fig. 9. The performance of simulation is quite good, which means that the simulation results are similar in trends to the experimental results. The minimum stress for simulation results is -1458 MPa, which is very close to the minimal experimental result -1508 MPa. As discussed previously, the growth strain and the viscoplastic strain at high temperature play important roles in this system and this numerical model is suitable for simulating this kind of systems. Once again, the simulation is not perfect and the delay of the inflection time may be caused by the different conditions between the experiments and simulation for the temperature increase phase.

5.3 Oxidation at 1000°C for 1h

By using the parameters in Table 1, the mesh and geometry of Fig. 2, the simulation results are obtained and the stress distribution curves along the center path are plotted.

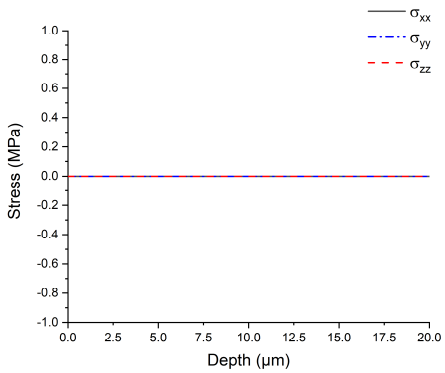

(a) end of phase 1 : temperature increase

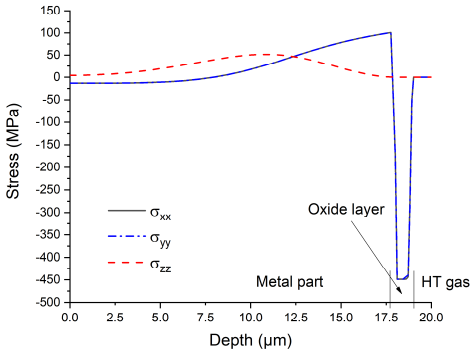

(b) end of phase 2 : constant temperature

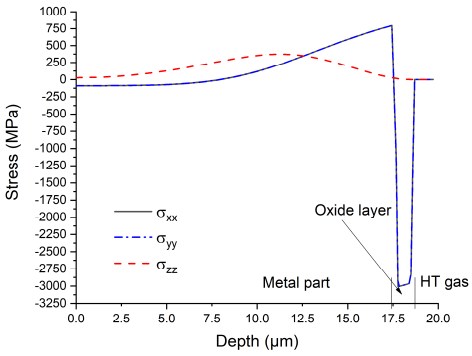

(c) end of phase 3 : temperature decrease

Figure 10. The distribution of stress components at the end of phase 1 (a), at the end of phase 2 (b), and at the end of phase 3 (c); in the deformed configuration

Fig. 10 indicates the stress distribution along axis z. For Figs. 10 (a) to (c), the interface of metal/oxide is at depth around 17.5 μm. The results show that the stress in the metal layer is mainly in tension and in the oxide layer is in compression. At the end of phase 2, the maximum absolute value for stress in the oxide layer is 449 MPa and in the metal layer is 101 MPa. At the end of phase 3, room temperature, the maximum absolute value for stress in the oxide layer is 3009 MPa and in the metal layer is 795 MPa.

In order to compare with the results obtained in the work of Tao [16], for material Ni30Cr and oxidized at 1000°C for 7.4h, the time-dependent stress is plotted. It is shown the time-dependent stresses of the first one hour for the experimental and simulation results.

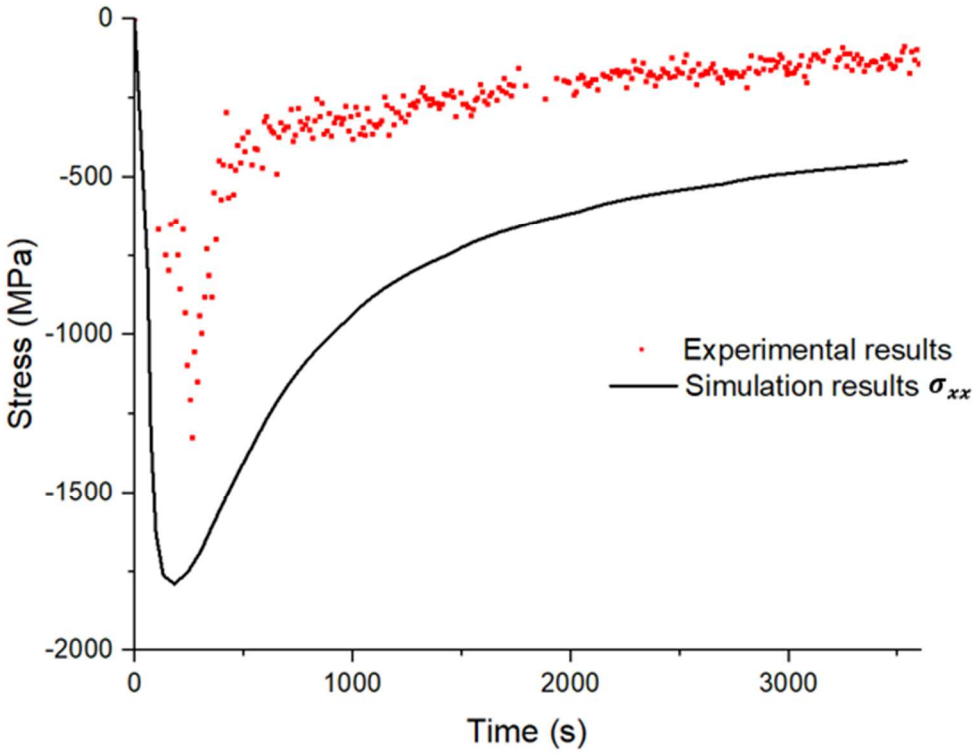

Figure 11. Time evolution of stress $\boldsymbol{\sigma_{xx}}$ for isothermal condition at 1000°C

Fig. 11 shows that the simulation results have the same trend as the experimental results. However, the simulation results are now lower than the experimental results. For the delay of the inflection time, it shows here a good synchronism for the simulation results and experimental results, around 250 s. For the minimum stress, it is -1788 MPa for the simulation results and -1324 MPa for the experimental results. Overall, this simulation proved its suitability for estimating stresses at isothermal loading.

5.4 Influence of oxidation temperature and oxidation time

It is possible to observe the influence of temperature on the different stress components. This is plotted in Figs. 12 and 13. Because the calculations at 1000°C are not at the same duration for the second phase, it is also interesting to see the influence of this time process on the results. We have plotted the cases for 1000°C for 1h then 5h of oxidation time during the second phase.

We have systematically plotted the results at the end of phase 2 (figures a) and at the end of phase 3 (figures b). Whatever the component is, the curves keep the same trends. However, the amplitude is 10 times higher.

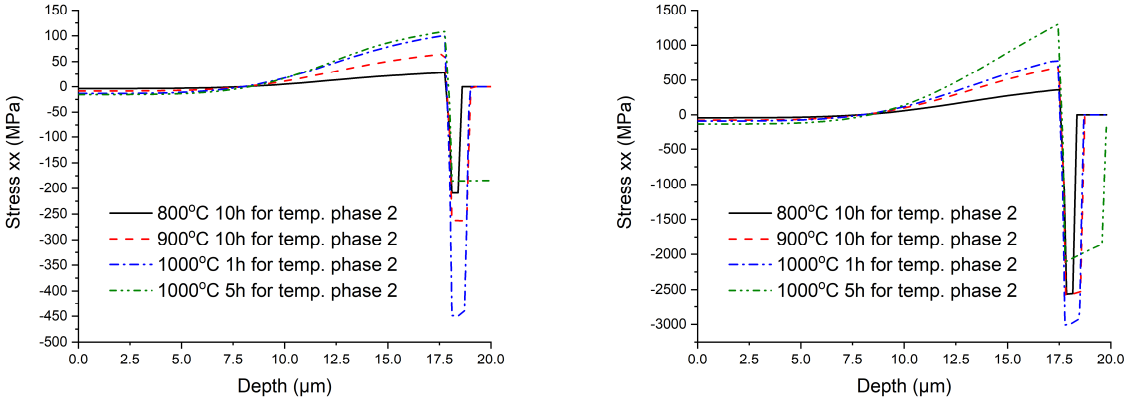

(a) end of phase 2 : constant temperature (b) end of phase 3 : temperature decrease

Figure 12. Evolution of $\boldsymbol{\sigma_{xx}}$ as a function of the depth for the different temperatures (a) at the end of the isothermal oxidation temperature and (b) after cooling at ambient temperature

For the metal stress component $\boldsymbol{\sigma_{xx}}$ (Fig12a or b), the values are slightly negative and increase significantly to be positive near the metal/oxide interface. The stress is higher for the highest temperature. For 1000°C, the duration of the isothermal oxidation increases the value of the stress in the metal, at the end of phase 2 or 3. The maximum of this stress component is always at the metal/oxide interface.

For the oxide stress component $\boldsymbol{\sigma_{xx}}$ (Fig12a or b), the values are systematically negative and almost constant with the depth. It is difficult to identify a gradient of stress in the oxide. The stress is higher for 1000°C only for an isothermal duration of 1h. For 5h at 1000°C, the oxide layer thickness is significantly greater (two times), then the level of stress is observed lower (around two times). This is consistent with mechanical balance [9] such that $\int_0^{h_m} \boldsymbol{\sigma_{xx}(z)dz} = -\int_{h_m}^{h_m+h_{ox}} \boldsymbol{\sigma_{xx}(z)dz} \approx -\boldsymbol{\sigma_{xx,ox}h_{ox}}$. Because the distribution of stress in the metal at 1000°C is similar for 1h and 5h, then the oxide stress times the oxide thickness is roughly constant. Then increasing the thickness of a given value leads necessarily to decrease the oxide stress of the same value.

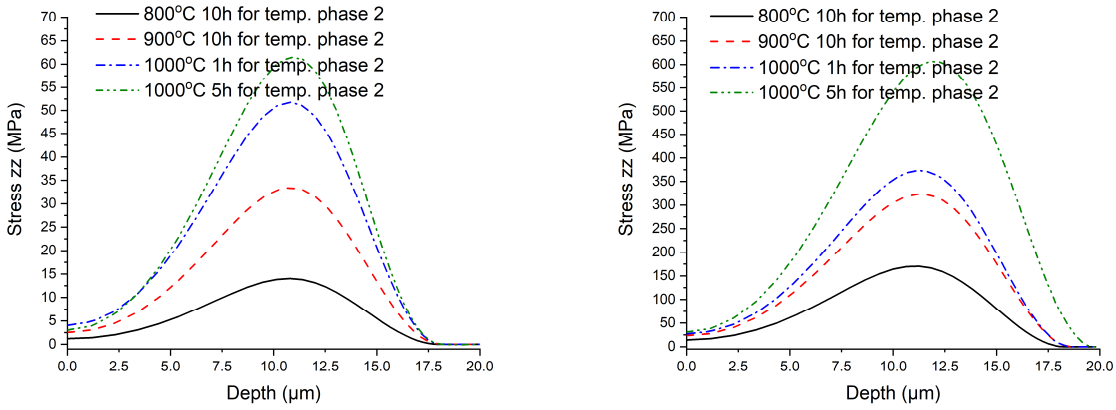

(a) end of phase 2 : constant temperature (b) end of phase 3 : temperature decrease

Figure 13. Evolution of $\boldsymbol{\sigma_{zz}}$ as a function of the depth for the different temperatures (a) at the end of the isothermal oxidation temperature and (b) after cooling at ambient temperature

For the metal stress component $\boldsymbol{\sigma_{zz}}$ (Fig12a or b), the values are positive and evolve continuously including at the metal/oxide interface. The values are of the same order of magnitude than the component $\boldsymbol{\sigma_{xx}}$, with a different distribution. The maximum of this stress component $\boldsymbol{\sigma_{zz}}$ is at around 7 µm under the interface in the metal. In the oxide, the stress is almost zero, except for the end of phase 3 for 1000°C at 5h of isothermal oxidation.

5.5 Evolution of the stress as function of y direction

It is also interesting to see details of the dependence along y of the results. For such a goal, two new paths have been created from coordinates in µm (10, 0, 15) to (10, 20, 15) in the metal, and from coordinates in µm (10, 0, 18) to (10, 20, 18) in the oxide. Both paths are separated by 3 µm height along z direction. The results are plotted in Figs. 14, 15 and 16.

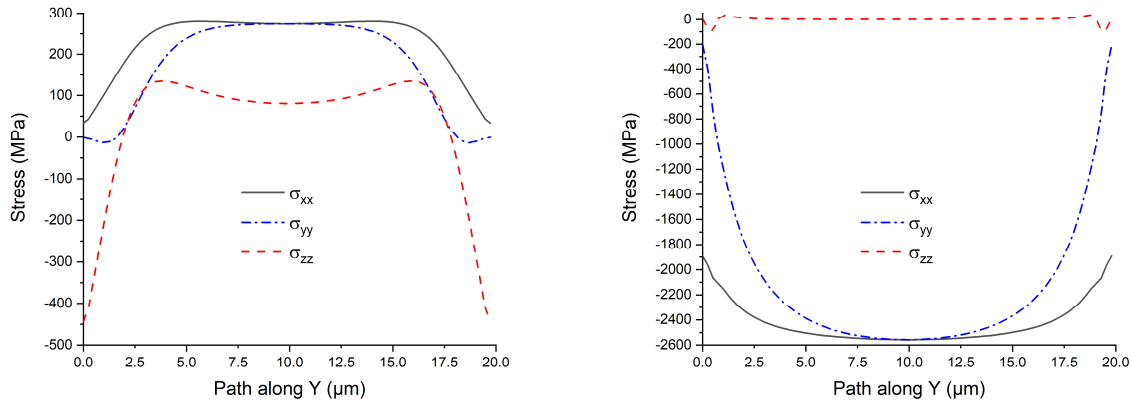

(a) 800°C in the metal (b) 800°C in the oxide

Figure 14. Evolution of stress along y direction at 800°C (a) in the metal and (b) in the oxide, at the end of the phase of decreasing temperature; in the deformed configuration

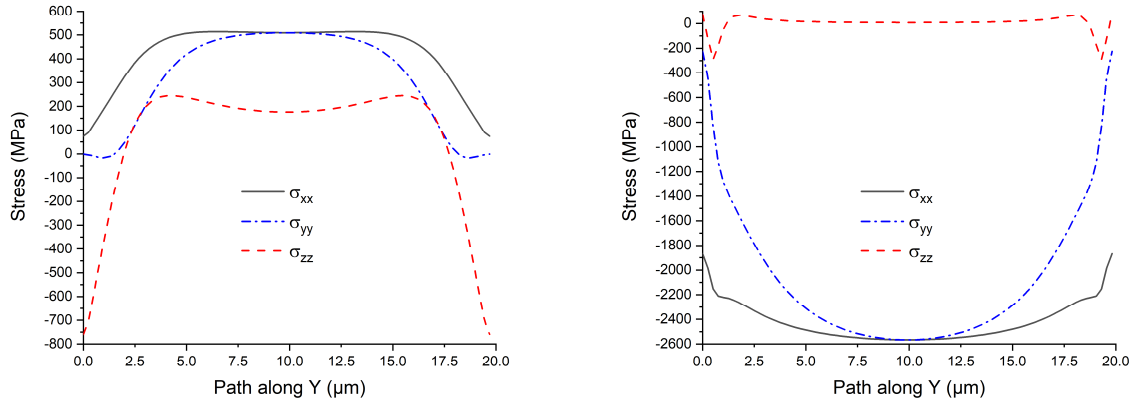

(a) 900°C in the metal (b) 900°C in the oxide

Figure 15. Evolution of stress along y direction at 900°C (a) in the metal and (b) in the oxide, at the end of the phase of decreasing temperature; in the deformed configuration

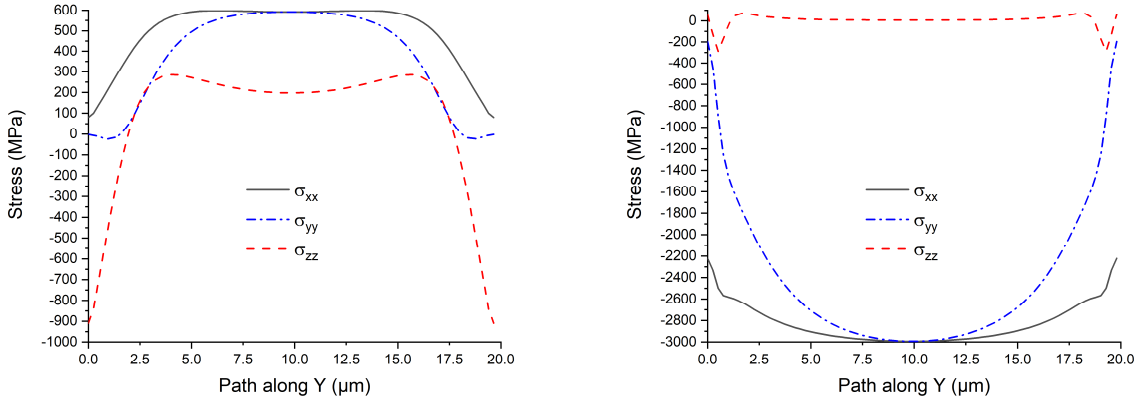

(a) 1000°C in the metal (b) 1000°C in the oxide

Figure 16. Evolution of stress along y direction at 1000°C (a) in the metal and (b) in the oxide, at the end of the phase of decreasing temperature; in the deformed configuration

In these figures, we can observe border effects that are significant up to 5 μm in the domain of calculations. For the metal (Figs. 14a, 15a and 16a), except from the border, the stress components are in tension with values around hundreds of MPa. The $\boldsymbol{\sigma_{zz}}$ component is systematically smaller than the other components. For the oxide (Figs. 14b, 15b and 16b), the stress components are in compression. The values for $\boldsymbol{\sigma_{xx}}$ and $\boldsymbol{\sigma_{yy}}$ are between 2.4 and 3 GPa, whereas the value is close to 0 for the $\boldsymbol{\sigma_{zz}}$ component. As expected for a thin oxide layer, we have an in-plane stress state, whereas it is not in the metal.

In order to verify the stress distribution in oxide layer and in metal layer, the simulation results can be compared with experimental results for the system Cr_2O_3/NiCr.

For the stress in oxide layer, the comparison is shown in Table 2.

Table 2. Comparison of residual stresses at room temperature in oxide layer

Simulation results (see for example in Fig. 12b)		Results from articles [9,18]					
Sample	σ_{ox} (GPa)	Sample	σ_{ox} (GPa)	Sample	σ_{ox} (GPa)	Sample	σ_{ox} (GPa)
1000°C_1h	-3.01	1000°C_1h	-3.05	1000°C_3h	-2.60, − 2.35, − 3.05		
1000°C_5h	-2.1	1000°C_5h	-3.04			1000°C_18h	-3.00
800°C_10h	-2.56	800°C_10h	-2.61	800°C_3h	-1.56	800°C_18h	-1.84
900°C_10h	-2.58	900°C_10h	-2.77	900°C_3h	-1.94	900°C_18h	-2.40, − 2.10, − 2.50

Table 2 shows the comparison between simulation results of residual stresses in oxide layer at room temperature and the results found in other articles concerning the same material, for different conditions of oxidation temperature and oxidation time, after temperature cooling (end of phase 3). It shows clearly that the values are all with the same orders of magnitude. Comparing more deeply the results under the same experimental conditions, it indicates that the simulation results is extremely similar to the results found in previous works, except oxidation at 1000°C for 5h that presents a higher discrepancy. The simulation results for the sample 1000°C_5h is lower than the other results, which may be caused by the relaxation that is much stronger in the present simulation. The viscoplastic phenomena remain thus to be further studied in future works. With the other oxidation conditions, the simulation results are generally a little bit bigger than the experimental results found in other articles, with a maximum difference of 7% at 900°C for 10h.

The comparison of stress in metal layer is shown in Table 3.

Table 3. Comparison of residual stresses at room temperature in metal layer

Simulation results (see for example in Fig. 12b)		Results from article [9]	
Sample	σ_{metal} (MPa)	Sample	σ_{metal} (MPa)
1000°C_1h	323.1	1000°C_1h	452.3

1000°C_5h	467.1	1000°C_5h	388.8
800°C_10h	145.2	800°C_10h	151.5
900°C_10h	267.7	900°C_10h	41.7

In the article [9], experimental stress distribution were determined and present gradients in the metal near the metal/oxide interface. It is worth noting that for the simulation results, such a non-constant distribution has a similar trend, but the gradient is less significant. In order to make quantitative comparison, one can make an averaging process. For example, the average stress in metal layer in [9] can be calculated as the asymptotic mean value far from the interface. In the present simulation, we can also calculate the average stress in metal layer as proposed in Table 3. The comparison shows that they are at the same order of magnitude. Except for the sample 900°C_10h, the results of the other samples are quite close. Difference seems more important than for the oxide. However, we should keep in mind that for the experimental results, it is influenced by experimental environment and calibration leading to uncertainties. In the considered work performed in [9], the uncertainty was around ±100 MPa, such that differences between experimented and simulated values in metal are in fact quite small. For both simulation results and experimental ones, they indicate a tension stress in metal layer and the averaged results are comparable, as well as the presence of a stress gradient in the metal near the interface in both experimental and simulation results.

5.6 General discussion

It is interesting to draw some general consequences when observing the evolution of stress as function of the depth in Figs. 6, 8 and 10. First, stress in the metal is mainly in tension, whereas stress in the oxide is systematically in compression. Second, the effects of the two sources of stress, oxide growth and thermal mismatch, lead to the same tendencies. Difference is only observed on the value of the stress especially in the oxide, where it reaches few GPa at the end of temperature decrease. Third, in the metal, during the isothermal phase or during the decreasing phase, the stress components $\boldsymbol{\sigma_{xx}}$ and $\boldsymbol{\sigma_{zz}}$ present similar values, whereas they have not strictly the same tendencies. This last observation is consistent with the experimental observations performed in [9] in the metal by use of X-ray diffraction method with transmission configuration. According to experimental uncertainties, it is thus possible to approximate the two components in the metal when no other information are available such that $\boldsymbol{\sigma_{xx}} \approx \boldsymbol{\sigma_{zz}}$. Fourth, along the considered path, the system presents an isotropic stress state with superimposition of components $\boldsymbol{\sigma_{xx}}$ and $\boldsymbol{\sigma_{yy}}$. All these conclusions are similar for all the temperatures.

From evolution of stress versus oxidation time as seen in Fig. 7, 9 and 11, it is also possible to draw general consequences. First, during the isothermal phase, the numerical results present similar evolutions that are confirmed in other works [5] where growth strain is balanced by relaxation effect with an inflection time. Second, experimental results are close to the simulation, but not strictly equivalent. The differences can be observed of two kinds, either the inflexion time is slightly shifted, or the amplitude of the numerical results is a little bit bigger (in absolute value). There would be several ways to improve the coincidence/synchronism between simulation results and experimental results. One is to change the parameters, which can be done by an optimization process considering simultaneously experimental results depending on both space and time. We could also change the oxidation conditions for the temperature-increasing phase. We have already mentioned that some behaviors in this phase have not been taken into account. Both approaches will be studied in future works.

6. Conclusions

This article focuses on the development of a spacetime numerical model for prediction of the stress generated in high temperature oxidation, during isothermal conditions then during the cooling process. The numerical simulation results are compared to the time–dependent stresses for oxide layer, and the residual stress at room temperature for oxide layer, by use of a full thermomechanical model including also growth and chromium diffusion phenomena. The latter were identified to have a significant influence on the development of strain and stress in the metal during isothermal conditions. The performed simulations confirms such a fact.

The sources of stress are eventually and mainly related to the growth of oxide layer during isothermal oxidation and to the thermal mismatch during the cooling process. The oxide layer is subjected to high compressive stresses of the order of 2-3 GPa at room temperature after the cooling process. The stress in the oxide is roughly constant in the oxide along the depth and presents border effects along x and y directions. The stress in the metallic substrate remains low, which is of the order of a few MPa and their maximum absolute values are also at the metal-oxide interface for the $\boldsymbol{\sigma_{xx}}$ component, whereas the maximum value is few µm under the interface for the $\boldsymbol{\sigma_{zz}}$ component.

The results of these simulations have been also compared with experimental observations, which show a similar tendency with the time–dependent stresses for oxide layer. During the isothermal conditions, the absolute value of stress increases at the beginning of oxidation, then it decreases because of the creep phenomena at high temperature. After the cooling process, the stress increases largely, which is due to the difference of thermal expansion coefficients between the oxide and metal layer of the present suited system, as expected.

An advantage of this simulation is also to propose a spatial stress distribution that enables to localize the amplitude of stress, especially at the metal/oxide interface that plays an important role for the stress evolution and integrity of the oxide layer. This aspect could be investigated by taking into account of two-dimensional or non-linear phenomena related to the damage of such systems to calculate lifetime from the present spacetime stress distributions.

References

[1] M. Schütze, Protective Oxide Scales and Their Breakdown, NJ, 1991.
[2] P. Kofstadt, High Temperature Corrosion, London, 1998.
[3] A.M. Huntz, B. Pieraggi, Oxydation des matériaux métalliques, Hermès Science, Paris, 2003.
[4] B. Panicaud, J.-L. Grosseau-Poussard, Z. Tao, F. Rakotovao, G. Geandier, P.-O. Renault, P. Goudeau, N. Boudet, N. Blanc, Frequency analysis for investigation of the thermomechanical mechanisms in thermal oxides growing on metals, Acta Mech. 228 (2017) 3595–3617. https://doi.org/10.1007/s00707-017-1899-z.
[5] Z.J. Tao, F. Rakotovao, J.L. Grosseau-Poussard, B. Panicaud, Determination of Stress Fields and Identification of Thermomechanical Parameters in a Thermally Grown Oxide under Thermal Cycling Loadings, Using Advanced Models, AMR. 996 (2014) 896–901. https://doi.org/10.4028/www.scientific.net/AMR.996.896.
[6] Z. Wang, J.-L. Grosseau-Poussard, B. Panicaud, G. Geandier, P.-O. Renault, P. Goudeau, N. Boudet, N. Blanc, F. Rakotovao, Z. Tao, Viscoplasticity and growth strain parameters identification by full modelling optimization during the high temperature oxidation of Ni28Cr modified by the reactive element yttria or zirconium, Computational Materials Science. 180 (2020) 109689. https://doi.org/10.1016/j.commatsci.2020.109689.
[7] Z. Wang, J.-L. Grosseau-Poussard, B. Panicaud, G. Geandier, P.-O. Renault, P. Goudeau, N. Boudet, N. Blanc, F. Rakotovao, Z. Tao, Determination of Residual Stresses in an Oxidized Metallic Alloy under Thermal Loadings, Metals. 8 (2018) 913. https://doi.org/10.3390/met8110913.
[8] B. Panicaud, J.-L. Grosseau-Poussard, M. Kemdehoundja, J.-F. Dinhut, Mechanical features optimization for oxide films growing on alloy, Computational Materials Science. 46 (2009) 42–48. https://doi.org/10.1016/j.commatsci.2009.02.003.
[9] Z. Wang, J.-L. Grosseau-Poussard, G. Geandier, B. Panicaud, Stress distribution in depth of NiCr + Cr_2O_3 systems using high-energy synchrotron X-rays in transmission mode, Journal of Alloys and Compounds. (2021) 159958. https://doi.org/10.1016/j.jallcom.2021.159958.
[10] B. Panicaud, J.L. Grosseau-Poussard, J.F. Dinhut, General approach on the growth strain versus viscoplastic relaxation during oxidation of metals, Computational Materials Science. 42 (2008) 286–294. https://doi.org/10.1016/j.commatsci.2007.07.017.
[11] A.M. Huntz, G.C. Amiri, H.E. Evans, G. Cailletaud, Comparison of Oxidation-Growth Stresses in NiO Film Measured by Deflection and Calculated Using Creep Analysis or Finite-Element Modeling, (n.d.) 23.
[12] N Kikuchi, JT Oden, Contact problems in elasticity: a study of variational inequalities and finite element methods, 1988
[13] Thomas J. R. Hughes, The Finite Element Method: Linear Static and Dynamic Finite Element Analysis, 2012
[14] Z. Zhuang, ABAQUS finite element based analysis and application (in Chinese), Tsinghua University, 2009.
[15] http://130.149.89.49:2080/v2016/books/sub/default.htm?startat=ch01s01asb44.html#sub-rtn-uumat
[16] Z. Tao, Etude expérimentale et modélisation des caractéristiques mécaniques d'une couche d'oxyde sous charges thermiques. PhD thesis, Université de Technologie de Troyes, Troyes, 2018.

[17] M. Guerain, Contribution à l'étude des mécanismes de relaxation de contraintes dans les films de chromine formés sur Ni-30Cr et Fe-47Cr : approche multi-échelle par spectroscopie Raman et microdiffraction Synchrotron, PhD Thesis, Université de La Rochelle, La Rochelle, France, 2012.
[18] F.N. Rakotovao, Relaxation des contraintes dans les couches de chromine développées sur alliages modèles (NiCr et Fe47Cr). Apport de la diffraction in situ à haute température sur rayonnement Synchrotron à l'étude du comportement viscoplastique. Effets d'éléments réactifs, PhD thesis, Université de La Rochelle, 2016.
[19] B. Panicaud, A. Hmima, C. Rampelberg, M. Ngom, F. Lebel, G. Geandier, T. Maurer, J.-L. Grosseau-Poussard, E. Guyot, J. Béal, J. Marae-Djouda, L. Le Joncour, A. Alhussein, Stress determination in a thermally grown oxide on Ni38Cr alloy by use of micro/nanogauge gratings, Materials Science and Engineering: A. 812 (2021) 141079. https://doi.org/10.1016/j.msea.2021.141079.
[20] J. Lemaitre, J.L. Chaboche, Mécanique des matériaux solides, Dunod, Paris, 2001.
[21] F. Rakotovao, B. Panicaud, J.L. Grosseau-Poussard, Z. Tao, G. Geandier, P.O. Renault, P. Girault, P. Goudeau, N. Blanc, N. Boudet, G. Bonnet, In situ Synchrotron X-Ray diffraction study of high-temperature stress relaxation in chromia scales containing the reactive element yttrium, Acta Materialia. 159 (2018) 276–285. https://doi.org/10.1016/j.actamat.2018.07.055.
[22] D.J. Baxter, K. Natesan, Mechanical considerations in the degradation of structural materials in aggressive environments at high temperatures Rev. High Temp. Mater., 5 (1983), pp. 149-250
[23] J.P. Poirier, Creep of Crystals: High-temperature Strain Processes Metals, Ceramics and Minerals Cambridge University Press, New York, 1985.
[24] S. Daghigh, Evolution des contraintes dans le système Ni70Cr30/Cr2O3 en fonction de la température. Etude in situ par diffraction des rayons X et modélisation = Evolution of stresses in Ni70Cr30/Cr2O3 system as a function of the temperature. In situ experiments with. PhD thesis, Paris XI Orsay University, 1996.
[25] D.R. Clarke, The lateral growth strain accompanying the formation of a thermally grown oxide, Acta Materialia. 51 (2003) 1393–1407. https://doi.org/10.1016/S1359-6454(02)00532-3.
[26] D. Fettre, Aspects mécaniques de l'oxydation haute température du zirconium: modélisation des champs de contrainte et suivi expérimental multi technique des endommagements, PhD Thesis, Université de Compiègne, Compiègne, France, 2017.
[27] A. Milton, S. Irene, Abramowitz and Stegun, U.S., 1964.
[28] D.P Whittle, D.J Evans, D.B Scully, G.C Wood, Compositional changes in the underlying alloy during the protective oxidation of alloys, Acta Metallurgica, Volume 15, Issue 9, 1967, Pages 1421-1430, https://doi.org/10.1016/0001-6160(67)90173-3.
[29] http://web.mit.edu/calculix_v2.7/CalculiX/ccx_2.7/doc/ccx/node27.html